Pressure-Induced Superconducting and Topological Phase Transitions in the RuX_2 (X=P, As, Sb) Family Compounds

CHEN Qun [1], WU Jue-fei [2], WANG Xiao-meng [1], DING Chi [1], HUANG Tian-heng [1], LU Qing [1], SUN Jian [1,3*]

1. National Laboratory of Solid State Microstructures, School of Physics, Nanjing University, Nanjing 210093, China
2. School of Physical Science and Technology, ShanghaiTech University, 393 Middle Huaxia Road, Shanghai 201210, China
3. Collaborative Innovation Center of Advanced Microstructures, Nanjing University, Nanjing 210093, China

Abstract: $RuSb_2$, as a sister material of thermoelectric material $FeSb_2$, has been extensively studied focusing on the comparisons with $FeSb_2$, however, the properties of $RuSb_2$ under pressure have not been surveyed thoroughly yet. In this work, we studied the properties of $RuSb_2$ under pressure and explored the similarities and differences of crystal and electronic structures between the Ru-pnictides partners RuP_2 and $RuAs_2$. Using the crystal structures search method together with first-principles calculations, we found that this family undergoes a serial of structural phase transitions: (I) For $RuSb_2$: $Pnnm \rightarrow I4/mcm \rightarrow I4/mmm$; (II) for RuP_2: $Pnnm \rightarrow I4_1/amd \rightarrow Cmcm$; (III) for $RuAs_2$: $Pnnm \rightarrow P\text{-}62m$. The newly found five phases are all energetically and dynamically stable at high-pressure and exhibit metallic properties. The four high pressure phases of $RuSb_2$ and RuP_2 can be quenched to zero pressure. The superconducting transition temperatures of $I4/mcm$ and $I4/mmm$ phases of $RuSb_2$ and $I4_1/amd$ and $Cmcm$ phase of RuP_2 are predicted to be approximately 7.3 K, 10.9 K, 13.0 K, and 10.1 K at 0 GPa, respectively. In addition, the $I4/mcm$ and $I4/mmm$ phases of $RuSb_2$ and the $I4_1/amd$ phase of RuP_2 exhibit non-trivial topological properties. Our studies illustrate that pressure is an effective way to tune the structural, electronic, and superconducting behavior of the Ru-pnictides compounds.

Key words: high-pressure; crystal structures search method; phase transition; superconductor; topological materials

CLC number: O469 **Document code:** A **DOI:** 10.13725/j.cnki.pip.2022.06.001

CONTENTS

Received date: 2022-10-7
* E-mail: jiansun@nju.edu.cn

I. INTRODUCTION

In recent decades, transition-metal pnictides have drawn lots of attention due to their unique physical properties, such as high-performance thermoelectricity in antimonides[1–6], unconventional superconductivity in arsenides[7–10], and topological properties in transition-metal oxypnictide[11–17]. Among them, the thermoelectric properties of transition-metal anti-

monides have been studied intensively. For example, $FeSb_2$ was observed to show extremely large thermopower and thermal conductivity at low temperatures[18–21], which was predicted to be originated from strong electron-electron correlation[18,22,23] and the phonon-drag effect[21]. In particular, the correlation strength is expected to increase with an increasing hybridization gap[23].

$RuSb_2$, as a sister material of $FeSb_2$, has been widely studied in recent decades. It is a narrow-gap semiconductor with an estimated gap of 0.26 eV, which is larger than that of $FeSb_2$. Although $RuSb_2$ is originally introduced as one of the thermoelectric candidates[24], the recent discovery indicates that its thermoelectric power is relatively small, which is one order of magnitude less than that of $FeSb_2$ at low temperatures. Nevertheless, the distinct Seebeck patterns of $RuSb_2$ and $FeSb_2$ draw lots of attention, with a particular Seebeck peak located at about 10 K, whereas the Seebeck coefficient of other thermoelectric materials usually decreases monotonically with increasing temperature[19]. Moreover, they have a different magnetic response[18]. Despite $RuSb_2$ being often used as a reference to study the multiple disparities with $FeSb_2$, focusing on the magnetic properties[25,26], not much work has been done on $RuSb_2$ itself.

As a fundamental thermodynamic parameter, pressure can be employed to control various properties of materials. It can cause a structural phase transition without contaminating materials with impurities[27–33], or synthesize new materials with exciting properties[34–41]. Pressure-driven structural phase transitions often reshape electronic structures accompanied by exotic physical properties. For instance, pressure can induce superconductivity transition in topological materials[42,43], and change the superconducting transition temperature of unconventional superconductors[44,45]. The transition-metal pnictides also exhibit novel properties under high pressure. For instance, $FeSb_2$ undergoes a phase transition from insulator to metal[46]; the thermoelectric properties of $CoSb_3$ can be enhanced by pressure[47].

Among thermoelectric materials, $RuSb_2$ has received little attention and deserves further studies. Given the similarities in crystal and electronic structures in other Ru-pnictides partners RuP_2 and $RuAs_2$, they can also be used for comparison. In this work, we employed pressure conditions up to 120 GPa to systematically study $RuSb_2$, RuP_2, and $RuAs_2$ compounds by crystal structure search method and first-principles calculations. We found that the RuX_2 (X=P, As, Sb) family compounds undergo a series of structural phase transitions. For $RuSb_2$: $Pnnm \rightarrow I4/mcm \rightarrow I4/mmm$; for RuP_2: $Pnnm \rightarrow I4_1/amd \rightarrow Cmcm$; and for $RuAs_2$: $Pnnm \rightarrow P\text{-}62m$. These newly predicted phases are energetically and dynamically stable at high pressure and even at ambient pressure. Then we studied their structural, electronic, and superconducting properties. When the spin-orbit coupling (SOC) effects were included, the $I4/mcm$, $I4/mmm$ phases of $RuSb_2$, and the $I4_1/amd$ phase of RuP_2 are identified to be topologically non-trivial. Moreover, the $I4/mcm$, $I4/mmm$ phases of $RuSb_2$ and the $I4_1/amd$, $Cmcm$ phases of RuP_2 exhibit superconductivity at zero pressure.

II. COMPUTATIONAL METHOD

To search for the most stable structures at a given pressure for $RuSb_2$, $RuAs_2$, and RuP_2, we used the machine-learning accelerated random structure searching code called Magus (machine learning and graph theory assisted universal structure searcher)[48,49] combined with the *ab-initio* calculations at 20, 40, 80, 100, and 120 GPa respectively. The Magus code has successfully predicted many high-pressure structures in different systems[41,50–54]. The maximum number of atoms in the simulation cell is up to 18. Structural optimizations and electronic structure calculations were carried out using the projector augmented wave (PAW)[55] method as implemented in the Vienna *ab-initio* simulation package (VASP)[56]. We employed the generalized gradient approximation (GGA) exchange-correlation density functional parameterized by Perdew-Burke-Ernzerhof (PBE)[57]. Electronic localization functions (ELF) calculated by VASP were displayed by Visualization for Electronic Structural Analysis (VESTA)[58]. The valence electrons of the pseudopotentials are $4d^{10}5s^25p^1$, $5s^25p^3$, $3s^23p^3$,

and $4s^24p^3$ for Ru, Sb, P, and As, respectively. Structures were relaxed with high accuracy with the plane-wave basis energy cutoff of 400 eV. Brillouin zone was meshed using the Monkhorst-Pack method with a spacing of $2\pi\times$ 0.25 nm^{-1}(the equivalent grid for $Pnnm$, $I4/mcm$, $I4mmm$, $I4_1/amd$, $Cmcm$, P-62m phase at the highest pressure are 9×12×10, 19×19×6, 16×16×8, 9 × 12 × 10, 12 × 12 × 14, and 14 × 14 × 10, respectively). In our atomic optimization, the tolerance of atomic force was set to 0.01 eV/nm. Phonon modes and frequencies of the structures were calculated by the VASP code, combining the PHONOPY code[59] which the phonon calculations were carried out with the finite-displacement method. We applied 2 × 2 × 2 supercells to calculate all structure's force constants. Quantum Espresso (QE) code[60] is used to calculate the electron-phonon coupling (EPC) constants and T_c using an energy cutoff of 120 Ry. The PBE exchange-correlation functional and norm-conserving pseudopotentials are used. We adopted 8×8×8 k-point mesh for charge self-consistent calculation, 16 × 16 × 16 k-point mesh for electron-phonon coupling (EPC) linewidth integration, and 4×4×4 q-point mesh for the dynamical matrix of $I4/mcm$ and $I4/mmm$ phase. The surface states were obtained by constructing the maximally localized Wannier functions (MLWFs)[61] and using the surface Green function approach[62], as implemented in the WANNIERTOOLS package[63].

III. RESULTS AND DISCUSSIONS

A. Predicted structures under high pressure

We performed structure searches of the RuX_2 (X= P, As, Sb) family at 20, 40, 80, 100, and 120 GPa, respectively. After tens of generations with more than three thousand structures are assessed at each pressure, we picked out five structures of the RuX_2 family, as shown in Fig. 1(b)-(f). The predicted crystal structures of the RuX_2 family under high pressure are in Table A1. The enthalpy-pressure relations of the RuX_2 family are plotted in Fig. 1(g)-(i). For $RuSb_2$ in Fig. 1(g), the phase transition from the $Pnnm$ to the predicted $I4/mcm$ (No. 140), as shown in Fig. 1(b) is predicted to occur around 30 GPa, followed by a phase transition to the predicted $I4/mmm$ (No. 139), as shown in Fig. 1(c), at about 105 GPa. The calculated volume-pressure (V–P) curve shows that the volume collapse is about 5.6 % and 1.2 % at ≈30 GPa and ≈105 GPa, respectively. These are first-order phase transitions. Compared with the $Pnnm$ phase, the predicted tetragonal phase $I4/mcm$ and $I4/mmm$ are stacked in Ru and Sb layers along the c-axis. The stacking sequence of the $I4/mcm$ phase is Sb-Ru-Sb, while the sequence of the $I4/mmm$ phase is Ru-Sb-Sb.

For $RuAs_2$ in Fig. 1(h), the $Pnnm$ transforms to the predicted P-62m in Fig. 1(d), at around 62 GPa, accompanying a volume collapse of about 4.8%. The predicted P-62m is hexagonal. Six As atoms surround Ru atoms and form hexagons.

For RuP_2 in Fig. 1(i), it undergoes two phase transitions. The transition from the $Pnnm$ to the predicted $I4_1/amd$ (No. 141) in Fig. 1(e) at around 49 GPa, following the transition to the predicted $Cmcm$ (No. 63) in Fig. 1(f) at around 118 GPa. The volume collapse is about 5.6 % and 1.2 % at ≈49 GPa and ≈118 GPa, respectively. The high-pressure phase $I4_1/amd$ is tetragonal and $Cmcm$ is orthorhombic. The P atoms are zig-zag patterns in both of the predicted structures. The zig-zag patterns form quasi-one-dimensional chains along the a or c-axis in the predicted $I4_1/amd$ in Fig. 1(e), and the Ru atoms are interspersed among these chains. Moreover, the zig-zag patterns form P atom layers in the predicted $Cmcm$, as shown in Fig. 1(f), sandwiching the Ru atoms.

Then we calculated the phonon dispersions of these predicted structures both at high pressures and ambient pressure. The phonon dispersion of the predicted $I4/mcm$ and $I4/mmm$ of $RuSb_2$ and the predicted $I4_1/amd$ and $Cmcm$ of RuP_2 have no imaginary curves within 120 GPa, suggesting their dynamical stability. But the predicted P-62m of $RuAs_2$ is stable above ≈40 GPa. Our results indicate that the predicted structures of $RuSb_2$ and RuP_2 are likely to be synthesized after the pressure release.

B. Electronic structures

As displayed in Fig. 2, we calculated the band structure and the projected density of states (PDOS)

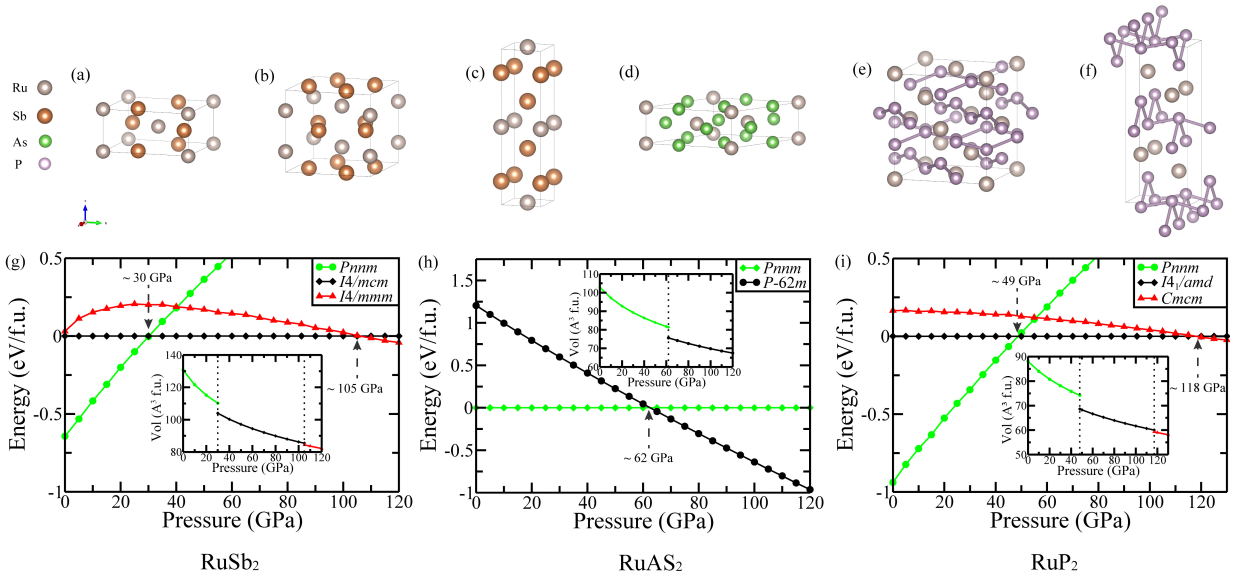

Fig. 1. The ground $Pnnm$ structure. The predicted structures (b) $I4/mcm$ and (c) $I4/mmm$ of $RuSb_2$, (d) P-62m of $RuAs_2$, (e) $I4_1/amd$ and (f) $Cmcm$ of RuP_2. The silver, brown, purple, and green spheres denote Ru, Sb, P, and As atoms, respectively. The pressure-dependent enthalpy difference of (g) $RuSb_2$ (relative to the $I4/mcm$), (h) $RuAs_2$ (relative to the P-62m), and (i) RuP_2 (relative to the $I4_1/amd$). The insets are the corresponding pressure-volume relation.

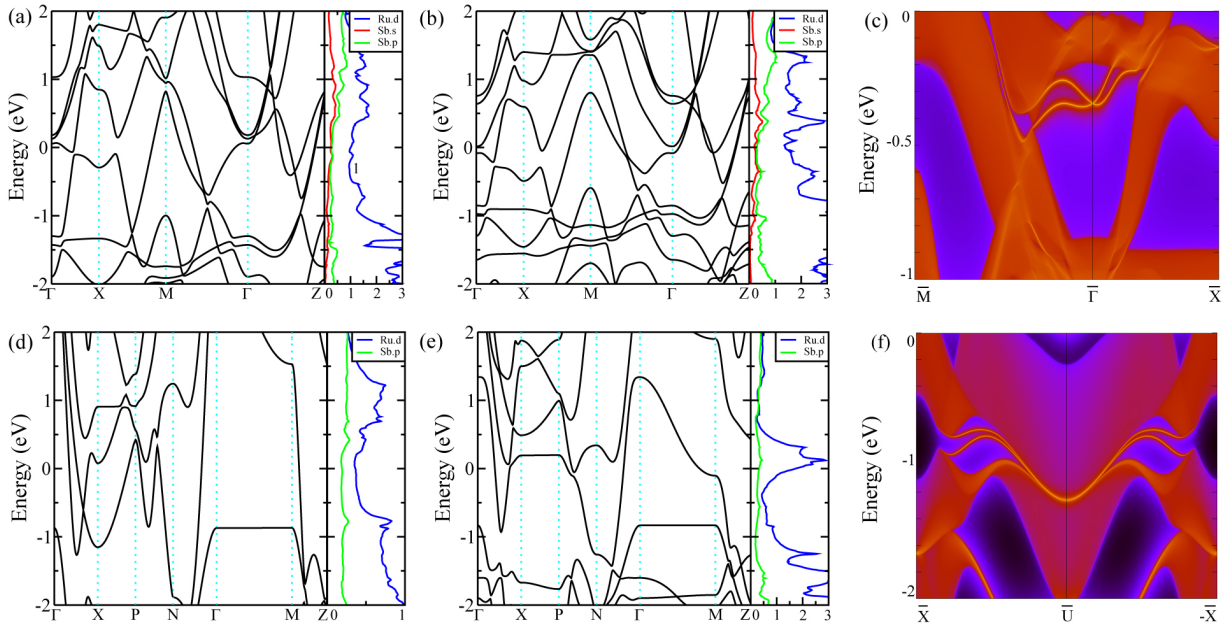

Fig. 2. The band structure of (a) $I4/mcm$ phase at 40 GPa with SOC, (b) $I4/mcm$ phase at 0 GPa with SOC. The surface state of (c) $I4/mcm$ phase at 0 GPa with SOC. The band structure of (d) $I4/mmm$ phase at 110 GPa with SOC, (e) $I4/mmm$ phase at 0 GPa with SOC. The surface state of (f) $I4/mmm$ phase at 0 GPa with SOC.

of the predicted $I4/mcm$ at 40 GPa [Fig. 2(a)] and 0 GPa [Fig. 2(b)] and the predicted $I4/mmm$ at 110 GPa [Fig. 2(d)] 0 GPa and [Fig. 2(e)] for $RuSb_2$ with SOC. The band structures of the predicted $I4/mcm$ and $I4/mmm$ have metallic features. The PDOS results indicate that the d electrons of the Ru atoms play a dominant role around the Fermi level. Comparing the PDOS at ambient pressure and high pressure of both predicted structures, the distribution of the d electrons is more localized around the Fermi level, such as the dominant peaks of the predicted $I4/mcm$ and $I4/mmm$ at ambient pressure, as shown in Fig. 2(b)

and (e). The increase of the DOS at the Fermi level may cause the elevation in superconductivity, which we will discuss in part III.C.

Besides, the band structures of both predicted phases at ambient pressure, as shown in Fig. 2(b) and (e), open up the energy gap on the high symmetry path. Thus, we performed the calculation of the topological invariance with the help of MLWFs. The symmetry indicators for the $I4/mcm$ phase are $Z_{2w,i=1,2,3} = 1$, $Z_2 = 1$, $Z_4 = 1$, $Z_8 = 1$, and the symmetry indicators for the $I4/mmm$ phase are $Z_{2w,i=1,2,3} = 1$, $Z_2 = 0$, $Z_4 = 2$, $Z_8 = 2$, indicating that both phases are topologically non-trivial. For further confirmation, we calculated their surface states with SOC, as shown in Fig. 2(c) for $I4/mcm$ and Fig 2(f) for $I4/mmm$. The red regions indicate the projected bulk band structure. We projected the band structures along k-path $\bar{\text{M}}$-$\bar{\Gamma}$-$\bar{\text{X}}$ for the $I4/mcm$. Dirac-type surface states appear at the energy ≈0.4 eV below the Fermi level around the $\bar{\Gamma}$ point. Analogous to the $I4/mcm$ phase, we projected the band structures along the k-point path $\bar{\text{X}}$-$\bar{\text{U}}$-$\bar{\text{X}}$ and find surface states around the $\bar{\text{U}}$ point, confirming that the $I4/mcm$ and $I4/mmm$ phases are topologically non-trivial at ambient condition.

As for $RuAs_2$, the band structures and the PDOS for the predicted P-62m around the transition point are in Fig. A1. It is topologically trivial and the d electrons of the Ru atoms make the main contribution around the Fermi level.

The band structure and the PDOS of the $I4_1/amd$ phase at 50 GPa and 0 GPa with SOC are plotted in Fig. 3(a) and (b). It has metallic features within 50 GPa, and the d electrons of the Ru atoms are dominant for the density of states around the Fermi level. The density of states near the Fermi level has a similar feature to the $RuSb_2$ phases. We also computed the symmetry indicators for the $I4_1/amd$ phase at ambient conditions, with the $Z_2 = 1$ and $Z_4 = 1$. Then we projected the band structures along the k-point path $\bar{\text{P}}$-$\bar{\Gamma}$-$\bar{\text{X}}$ and observe the topologically protected gapless surface states in Fig. 3(c). Dirac-type surface band appears at the energy of ≈0.4 eV above the Fermi level at $\bar{\Gamma}$ point, confirming that the $I4_1/amd$ phase is topologically non-trivial. The band structures of the predicted phases without SOC are plotted in Fig. A3.

C. Superconductivity

To study the potential superconductivity of the predicted phases of the RuX_2 family, we performed the EPC calculations at different pressures. Phonon dispersions, phonon density of states (PDOS), the corresponding Eliashberg spectral function $\alpha^2F(\omega)$ and the EPC parameter λ are calculated. The superconducting transition temperature T_c was estimated according to the Allen-Dynes modified McMillan formula:

$$T_c = \frac{\omega_{\log}}{1.2} \exp\left[\frac{-1.04(1+\lambda)}{\lambda - \mu^*(1+0.62\lambda)}\right], \quad (1)$$

with the typical Coulomb pseudopotential $\mu^* = 0.1$. The logarithmic averaged phonon frequencies ($\omega_{\log}$), and frequency-dependent EPC $\lambda(\omega)$ are obtained from the Eliashberg formalism.

Fig. 4(a) and (b) are the EPC calculation results of the predicted $I4/mcm$ of $RuSb_2$ at 0 GPa and 40 GPa, respectively. The EPC parameter λ for the predicted $I4/mcm$ at 40 GPa is 0.56 and T_c = 3.4 K, while the EPC parameter λ enhances to 0.94 and T_c = 7.3 K at ambient pressure. The Fermi surface of the $I4/mcm$ phases at 0 GPa is shown in Fig. A4. We can see that several electron pockets and hole pockets are distributed along with the high symmetry points, where the electron pocket around the Γ point and the hole pocket wrapped around the M point are mainly composed of 4d electrons in Ru atoms. Although we can observe the phonon softening behavior around M and Z points, as shown in Fig. 4(a), this part does not make enough contribution to the EPC parameter λ. As mentioned in part III.B, the DOS is more localized around the Fermi level for the predicted $I4/mcm$ at ambient pressure. This may suggest that the electron distribution contributes more to the enhancement of T_c than the softening behavior at M and Z points.

Fig. 4(c) and (d) are the EPC results of the predicted $I4/mmm$ of $RuSb_2$ at 0 GPa and 110 GPa, respectively. The EPC parameter λ is 1.46 at 0 GPa and 0.32 at 110 GPa, and the corresponding T_c is 10.9 K and 0.2 K, respectively. Its Fermi surface is plotted in Fig. A4. For $I4/mmm$ phase, there is an electron pocket around the Γ point and several electron pockets along the X-P path. Different from the $I4/mcm$ phase, phonon softening behavior is along the Brillouin

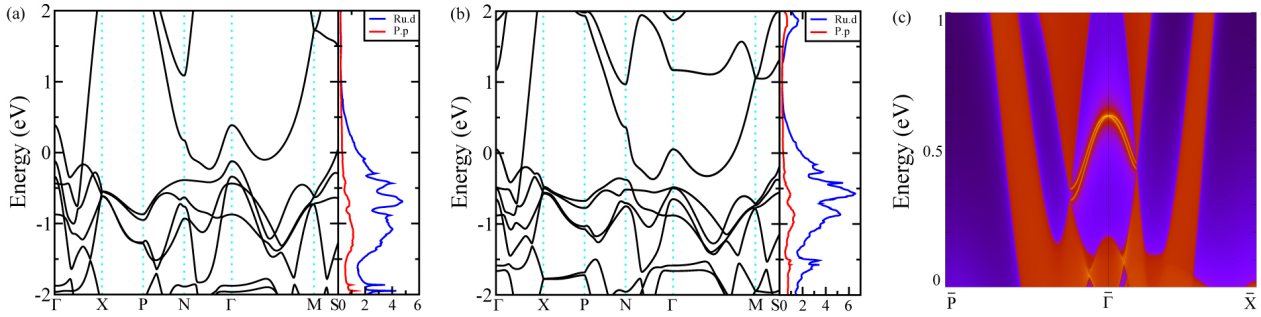

Fig. 3. The band structure of $I4_1/amd$ phase at (a) 40 GPa and at (b) 0 GPa with SOC. (c) The surface state of $I4_1/amd$ phase at 0 GPa with SOC.

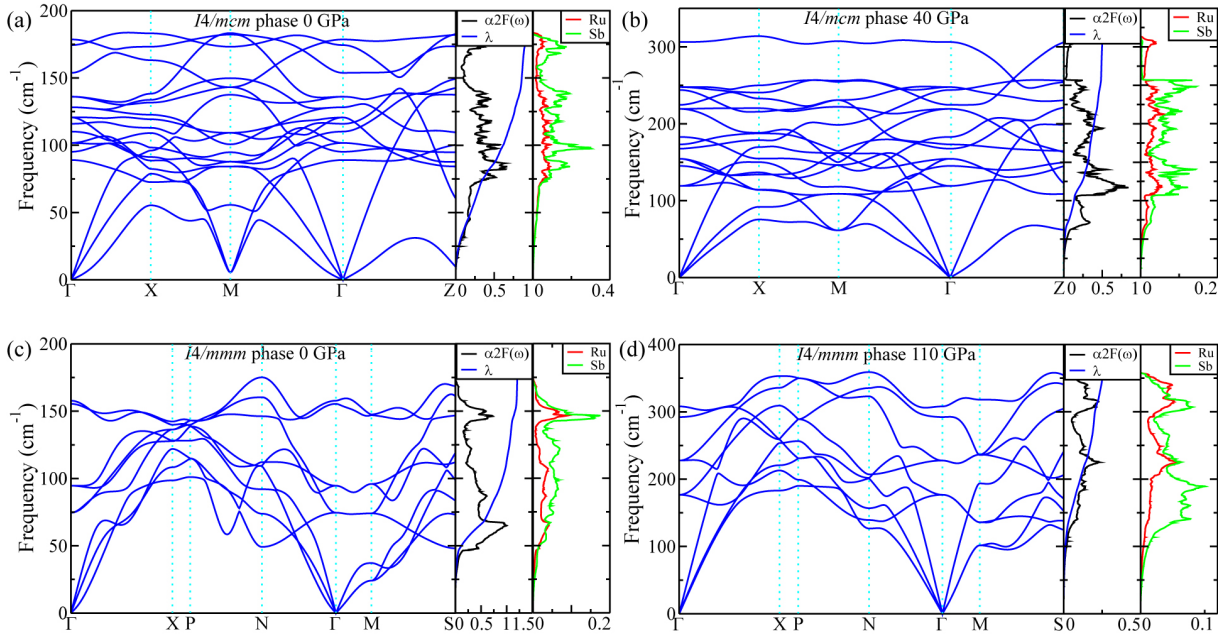

Fig. 4. Phonon dispersion curves, Eliashberg spectral functions $\alpha^2F(\omega)$ together with the electron-phonon integral $\lambda(\omega)$ and phonon density of states (PHDOS) for $I4/mcm$ phase at (a) 0 GPa, and (b) 40 GPa; and for $I4/mmm$ phase at (c) 0 GPa, and (d) 110 GPa, respectively.

path, such as Γ-X and P-N. There is a sharp increase of EPC parameter λ between 50 cm^{-1} and 75 cm^{-1}. Meanwhile, there is a localized peak in DOS at ambient pressure, while the DOS has little dispersion at 110 GPa , as shown in Fig. 2(e) and (f). Therefore, the enhancement of T_c is the comprehensive interactions between phonons and electrons. The λ, ω_{log}, and T_c results for the predicted structures of $RuSb_2$ are collected in Table I.

The EPC calculations of the predicted structures for RuP_2 are in Fig. 5 and their Fermi surface results are in Fig. A4. There are several electron and hole pockets distributed along the high symmetry points. For the $I4_1/amd$ phase, there are several electron pockets around the Γ point, A point, and S point. These

TABLE I. The electron-phonon coupling constant (λ), logarithmic average of phonon frequencies (ω_{log}), and estimated superconducting critical temperature (T_c) with the Coulomb potential (μ^*) of 0.1 for $I4/mcm$ and $I4/mmm$ phase of $RuSb_2$.

	λ	ω_{log} (cm^{-1})	T_c (K)
$I4/mcm$-0 GPa	0.94	116.51	7.3
$I4/mcm$-40 GPa	0.56	188.41	3.5
$I4/mmm$-0 GPa	1.46	97.5	10.9
$I4/mmm$-110 GPa	0.32	277.7	0.2

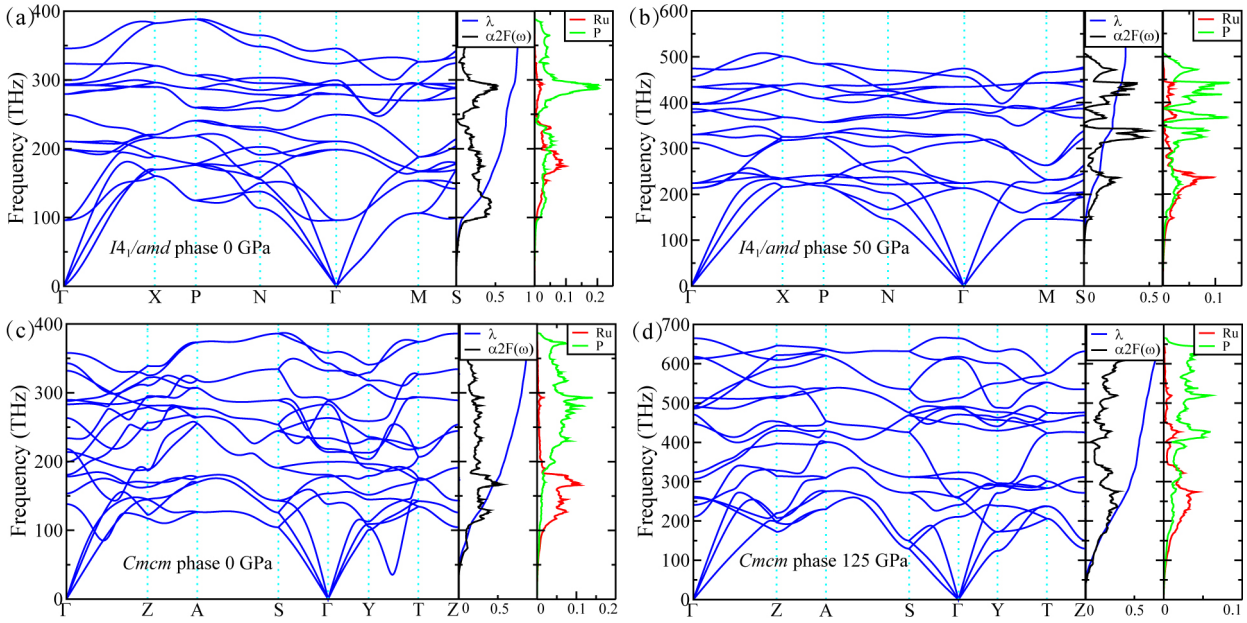

Fig. 5. Phonon dispersion curves, Eliashberg spectral functions $\alpha^2F(\omega)$ together with the electron-phonon integral $\lambda(\omega)$ and phonon density of states (PHDOS) for the $I4_1/amd$ phase of RuP_2 at (a) 0 GPa and (b) 50 GPa, and the $Cmcm$ phase of RuP_2 at (c) 0 GPa and (d) 125 GPa, respectively.

electron pockets are mainly composed of d_{yz}, d_{xz}, and $d_{x^2-y^2}$ electrons in Ru atoms. The EPC results of the predicted $I4_1/amd$ at 0 GPa and 40 GPa are plotted in Fig.5 (a) and (b). The EPC parameter λ is elevated from 0.43 at 40 GPa to 0.87 at ambient pressure, and the T_c is 2.4 K at 40 GPa and 13.0 K at ambient pressure. The phonon dispersions are analogous to the predicted $I4/mmm$ of $RuSb_2$. The phonon bands are in general softened along the Brillouin path, such as N-Γ-P, while the DOS around the Fermi level at ambient pressure is similar to that at 40 GPa, as shown in Fig. 3(a) and (b). Hence, we propose that phonons make more contributions to EPC.

As for the predicted $Cmcm$ phase, the EPC results at ambient pressure and 125 GPa are depicted in Fig. 5(c) and (d). The EPC parameter λ is 1.0 at ambient pressure and 0.38 at 125 GPa, with T_c = 10.1 K at ambient pressure and T_c= 1.2 K at 125 GPa. In analogous to the EPC results from the predicted $I4/mcm$ of $RuSb_2$, the softening behavior at ambient pressure along the Brillouin path Y-C and T-Y below 50 cm^{-1} does not have enough contribution to the EPC parameter. Moreover, the DOS is more localized around the Fermi level at ambient pressure than 125 GPa, as shown in Fig. A2. We assume that the electron distribution contributes more to the enhancement of T_c. The λ, ω_{log}, and T_c results for the predicted structures of RuP_2 are collected in Table II.

TABLE II. The electron-phonon coupling constant (λ), logarithmic average of phonon frequencies (ω_{log}), and estimated superconducting critical temperature (T_c) with the Coulomb potential (μ^*) of 0.1 for $I4/mcm$ and $Cmcm$ phase of RuP_2.

	λ	ω_{log} (cm^{-1})	T_c (K)
$I4_1/amd$-0 GPa	0.87	235.9	13.0
$I4_1/amd$-50 GPa	0.43	388.4	2.4
$Cmcm$-0 GPa	1.0	131.1	10.1
$Cmcm$-125 GPa	0.38	390.9	1.2

IV. CONCLUSIONS

In summary, using a machine-learning and graph theory accelerated crystal structure search package (Magus), we have investigated the pressure-induced phase transitions of the $RuSb_2$ family. It is found that the $RuSb_2$ family undergoes a series of transitions from the ambient ($Pnnm$) phase to several high-pressure phases: (I) For $RuSb_2$, from $Pnnm$ phase to a tetragonal $I4/mcm$ phase, then to a tetragonal $I4/mmm$

phase; (II) For RuP_2, from $Pnnm$ phase to a tetragonal $I4_1/amd$ phase, then to a tetragonal Cmcm phase; (III) For $RuAs_2$, from $Pnnm$ phase to a tetragonal P-$62m$ phase. Our calculations indicate that these phases are all stable at high-pressure. Except for the $RuAs_2$, all these phases can be recovered to ambient pressure. The $I4/mcm$ and $I4/mmm$ phases of $RuSb_2$ and the $I4_1/amd$ phase of RuP_2 are predicted to be topological metals, taking into acount the SOC effect. The superconducting transition temperature T_c of $RuSb_2$ and RuP_2 shows a tendency of decreasing with increasing pressure. At 0 GPa, the maximum T_c of $I4/mcm$ and $I4/mmm$ phases of $RuSb_2$ are 7.3 K and 10.9 K, and the T_c of the $I4_1/amd$ and $Cmcm$ phases of RuP_2 is 13.0 K and 10.1 K, respectively. We hope that this work will stimulate experimental efforts to realize them in the laboratory.

ACKNOWLEDGMENTS

J.S. gratefully acknowledges the financial support from the National Key R&D Program of China (grant nos. 2022YFA1403201), the National Natural Science Foundation of China (grant no. 12125404, 11974162, and 11834006), and the Fundamental Research Funds for the Central Universities. The calculations were carried out using supercomputers at the High Performance Computing Center of Collaborative Innovation Center of Advanced Microstructures, the high-performance supercomputing center of Nanjing University.

APPENDIX

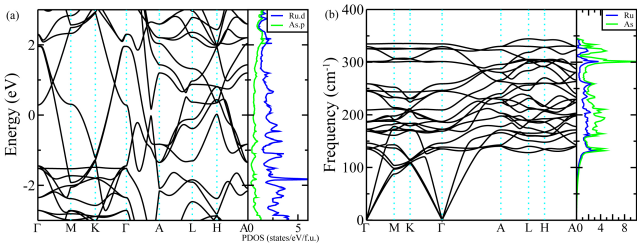

Fig. A1. $RuAs_2$ P-$62m$ band structure and PDOS at 65 GPa, phonon calculation at 65 GPa.

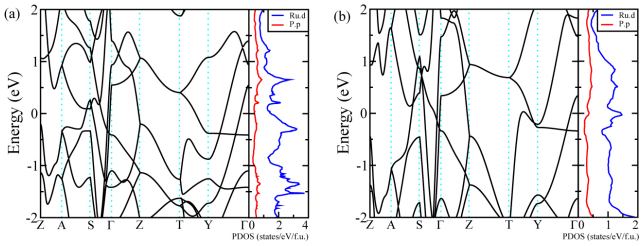

Fig. A2. RuP_2 $Cmcm$ band structure and PDOS at 0 GPa and 120 GPa.

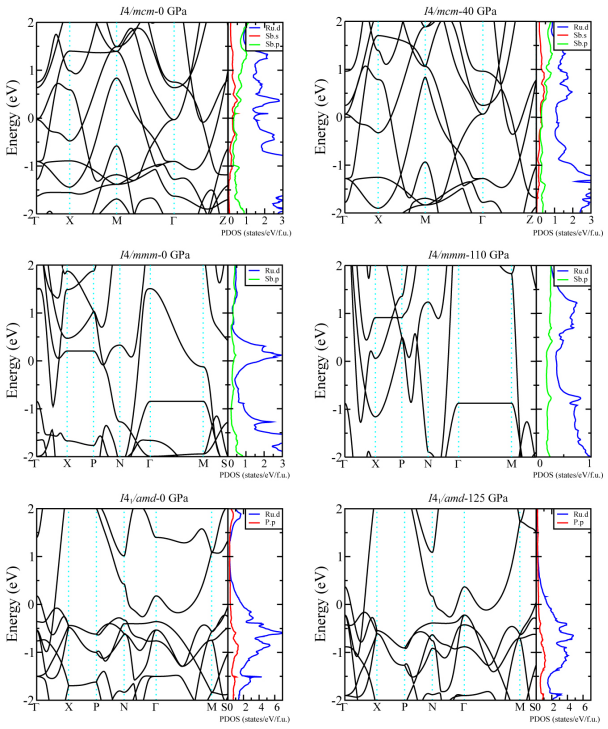

Fig. A3. Band structures of the predicted phases without SOC.

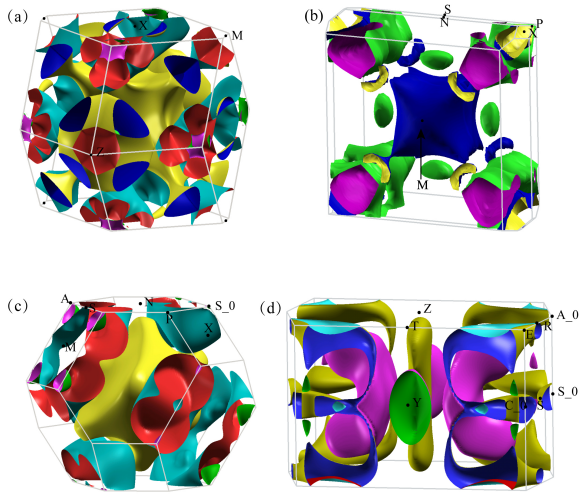

Fig. A4. The fermi surface of $RuSb_2$ and RuP_2 at 0 GPa. (a) $I4/mcm$ $RuSb_2$, (b) $I4/mmm$ $RuSb_2$, (c) $I4_1/amd$ RuP_2, and (d) $Cmcm$ RuP_2.

TABLE A1. The crystal structure of the predicted RuX_2 (X=Sb, As, P) family.

	Space-group	P (GPa)	Lattice parameters (nm)	α (°) β (°) γ (°)	Wyckoff position				
							x	y	z
$RuSb_2$	$I4/mcm$	40	0.601	90	Ru	4a	0.000 00	0.000 00	0.750 00
			0.601	90					
			0.554	90	Sb	8h	0.160 98	0.339 02	0.500 00
	$I4/mmm$	110	0.280	90	Ru	2b	0.000 00	0.000 00	-0.500 00
			0.280	90					
			1.062	90	Sb	4e	0.000 00	0.000 00	-0.151 17
$RuAs_2$	P-62m	40	0.695	90	Ru	2d	0.666 67	0.333 33	0.500 00
			0.695	90	Ru	1a	0.000 00	0.000 00	0.000 00
			0.288	120	As	3g	0.288 32	0.288 32	0.500 00
					As	3f	0.000 00	0.386 42	0.000 00
RuP_2	$I4_1/amd$	50	0.444	90	Ru	4a	0.500 00	0.000 00	0.750 00
			0.444	90					
			0.692	90	P	8e	0.000 00	0.000 00	0.335 80
	$Cmcm$	125	0.263	90	Ru	4c	-0.500 00	0.196 38	-0.250 00
			1.066	90	P	4c	-0.500 00	-0.474 25	-0.250 00
			0.416	90	P	4c	-0.500 00	0.128 31	-0.750 00

REFERENCES

[1] SHI X, YANG J, SALVADOR J R, et al. Multiple-filled skutterudites: high thermoelectric figure of merit through separately optimizing electrical and thermal transports[J], J. Am. Chem. Soc., 2011, 33 (20): 7837.

[2] SALES B C, MANDRUS D, CHAKOUMAKOS B C, et al. Filled skutterudite antimonides: electron crystals and phonon glasses[J]. Phys. Rev. B, 1997, 56: 15081.

[3] SALES B C, MANDRUS D, WILLIAMS R K. Filled skutterudite antimonides: a new class of thermoelectric materials[J], Science, 1996, 272: 1325.

[4] YU J J, XING Y F, HU C L, et al. Half-heusler thermoelectric module with high conversion efficiency and high power density[J]. Adv. Energy Mater., 2020, 10: 2000888.

[5] TAMAKI H, SATO H K, KANNO T. Isotropic conduction network and defect chemistry in $Mg_{3+\delta}Sb_2$-based layered zintl compounds with high thermoelectric performance[J]. Adv. Mater., 2016, 28: 10182.

[6] LIU Z Y, ZHU J L, TONG X, et al. A review of $CoSb_3$-based skutterudite thermoelectric materials[J]. J. Adv. Ceram., 2020, 9: 647.

[7] ROTTER M, TEGEL M, JOHRENDT D. Superconductivity at 38 K in the iron arsenide $(Ba_{1-x}K_x)Fe_2As_2$[J]. Phys. Rev. Lett., 2008, 101: 107006.

[8] MAZIN I I, SINGH D J, JOHANNES D M, DU M H. Unconventional superconductivity with a sign reversal in the order parameter of $LaFeAsO_{1-x}F_x$[J]. Phys. Rev. Lett., 2008, 101: 057003.

[9] PAGLIONE J, GREENE R L. High-temperature superconductivity in iron-based materials[J]. Nat. Phys., 2010, 6: 645.

[10] JOHNSTON D C. The puzzle of high temperature superconductivity in layered iron pnictides and chalcogenides[J]. Adv. Phys., 2010, 59: 803.

[11] SINGH S, WU Q, YUE C, et al. Topological phonons and thermoelectricity in triple-point metals[J]. Phys. Rev. Mater., 2018, 2: 114204.

[12] DU J H, LOU Z F, ZHANG S N, et al. Extremely large magnetoresistance in the topologically trivial semimetal α-WP_2[J]. Phys. Rev. B, 2018, 97: 245101.

[13] SHEN B, DENG X, KOTLIAR G, NI N. Fermi surface topology and negative longitudinal magnetoresistance observed in the semimetal $NbAs_2$[J]. Phys. Rev. B, 2016, 93: 195119.

[14] GHAEMI P, MONG R S K, MOORE J E. In-plane transport and enhanced thermoelectric performance in thin films of the topological insulators Bi_2Te_3 and Bi_2Se_3[J]. Phys. Rev. Lett., 2010, 105: 166603.

[15] BIANCHI M, GUAN D, BAO S, et al. Coexistence of thetopological state and a two-dimensional electron gas on the surface of Bi_2Se_3[J]. Nat. Commun., 2010, 1: 128.

[16] SHAO Y M, SUN Z Y, WANG Y, et al. Optical signatures of dirac nodal lines in $NbAs_2$[J]. Proc. Natl. Acad. Sci. U.S.A., 2019, 116: 1168.

[17] LV B Q, WENG H M, FU B B, et al. Experimental discovery of weyl semimetal TaAs[J]. Phys. Rev. X, 2015, 5: 031013.

[18] BENTIEN A, JOHNSEN S, MADSEN G K H, et al. Colossal seebeck coefficient in strongly correlated semiconductor $FeSb_2$[J]. Europhys. Lett., 2007, 80: 17008.

[19] SUN P, OESCHLERN, JOHNSEN S, et al. Huge thermoelectric power factor: $FeSb_2$ versus$FeAs_2$ and $RuSb_2$[J]. Appl. Phys. Express, 2009, 2: 091102.

[20] FUCCILLO M K, GIBSON Q D, ALI M N, et al. Correlated evolution of colossal thermoelectric effect and kondo insulating behavior [J]. APL. Mater., 2013, 1: 062102.

[21] TAKAHASHI H, OKAZAKI R, ISHIWATA S, et al. Colossal seebeck effect enhanced by quasi-ballistic phonons dragging massive electrons in $FeSb_2$[J]. Nat. Commun., 2016, 7: 12732.

[22] GIPPIUS A A, OKHOTNIKOV K S, BAENITZ M, SHEVELKOV A V. Band structure calculations and magnetic relaxation in correlated semiconductors $FeSb_2$ and $RuSb_2$[C]. Moscow(RU): Magnetism and magnetic materials, 2009.

[23] HONG S, GHAEMI P, MOORE J E, PHILLIPS P W. Tuning thermoelectric power factor by crystal-field and spin-orbit couplings in kondo-lattice materials [J]. Phys. Rev. B, 2013, 88: 075118.

[24] CAILLAT T, BORSHCHEVSKY A, FLEURIAL J P. Thermoelectric properties of a new semiconductor: $RuSb_2$[C]. New Mexico(USA): AIP Conference Proceedings, 1993.

[25] ZHANG L, WANG Y, CHANG H, High positive mr and energy band structure of $RuSb_2$[J]. Materials, 2020, 13: 3159.

[26] CHANG H, GUI X, HUANG S L, et al. Mn-induced ferromagnetism and enhanced thermoelectric properties in $Ru_{1-x}Mn_xSb_{2+\delta}$[J]. New J. Phys., 2019, 21: 033008.

[27] ZHOU Y H, LU P C, DU Y P, et al. Pressure-induced new topological weyl semimetal phase in TaAs[J]. Phys. Rev. Lett., 2016, 117: 146402.

[28] EFTHIMIOPOULOS I, LIU Z T Y, KUCWAY M, et al. Pressure-induced phase transitions in the $CdCr_2Se_4$ spinel[J]. Phys. Rev. B, 2016, 94: 174106.

[29] ELGHAZALI M A, NAUMOV P G, MU Q, et al. Pressure-induced metallization, transition to the pyrite-type structure, and Superconductivity in Palladium Disulfide PdS_2[J]. Phys. Rev. B, 2019, 100: 014507.

[30] WANG X, CHEN T, COGOLLO-OLIVO B H, et al. Pressure-induced structural and electronic transitions in InTeI[J]. Phys. Rev. B, 2021, 104: 064104.

[31] WANG X M, WU J F, WANG J H, et al. Pressure-induced structural and electronic transitions in bismuth iodide[J]. Phys. Rev. B, 2018, 98: 174112.

[32] HOU M Q, ZHANG Q, TAO R B, et al. Temperature-induced amorphization in $CaCO_3$ at high pressure and implications for recycled $CaCO_3$ in Subduction Zones[J]. Nat. Commun., 2019, 10: 1963.

[33] YING J, PAUDYAL H, HEIL C, CHEN X J, et al. Unusual pressure-induced periodic lattice distortion in $SnSe_2$[J]. Phys. Rev. Lett., 2018, 121: 027003.

[34] CHEN T, GU Q Y, CHEN Q, et al. Prediction of quasi-one-dimensional superconductivity in metastable two-dimensional boron[J]. Phys. Rev. B, 2020, 101: 054518.

[35] WU J F, FENG Z L, WANG J H, et al. Ground states of Au_2Pb and pressure-enhanced superconductivity[J]. Phys. Rev. B, 2019, 100: 060103.

[36] YUAN J N, XIA K, WU J F, SUN J. High-energy-density pentazolate salts: CaN_{10} and BaN_{10}[J]. Sci. China Phys. Mech. Astron., 2021, 64: 218211.

[37] DROZDOV A P, EREMETS M I, TROYAN I A, et al. Conventional superconductivity at 203 Kelvin at high pressures in the sulfur hydride system[J]. Nature, 2015, 525: 73.

[38] DROZDOV A P, KONG P P , MINKOV V S, et al. Superconductivity at 250 K in lanthanum hydride under high pressures[J]. Nature, 2019, 569: 528.

[39] DEWAELE A, WORTH N, PICKARD C J, et al. Synthesis and stability of xenon oxides Xe_2O_5 and Xe_3O_2 under Pressure[J]. Nat. Chem., 2016, 8: 784.

[40] GAO H, SUN J, PICKARD C J, NEEDS R J. Prediction of pressure-induced stabilization of noble-gas-atom compounds with alkali oxides and alkali sulfides[J]. Phys. Rev. Mater., 2019, 3: 015002.

[41] LI CU, GAO H, HERRMANN A, et al. Plastic and superionic helium ammonia compounds under high pressure and high temperature[J]. Phys. Rev. X , 2020, 10: 021007.

[42] ZHANG J L, ZHANG S J, MENG H M, et al. Pressure-induced superconductivity in topological parent compound Bi_2Te_3[J]. Proc. Natl. Acad. Sci. USA, 2011, 108: 24.

[43] PAL S, ARORA R, ROYCHOWDHURY S, et al. Pressure-induced phase transitions in the topological crystalline insulator SnTe and its comparison with semiconducting SnSe: Raman and first-principles studies[J]. Phys. Rev. B. 2020, 101: 155202.

[44] CHEN K Y, WANG N N, YIN Q W, et al. Double superconducting dome and triple enhancement of T_c in the kagome superconductor CsV_3Sb_5 under high pressure[J]. Phys. Rev. Lett., 2021, 126: 247001.

[45] K. MUKASA, MATSUURA K, QIU M. et al. High-pressure phase diagrams of $FeSe_{1-x}Te_x$: correlation between suppressed nematicity and enhanced superconductivity[J]. Nat. Commun, 2021, 12: 381.

[46] MANI A, JANAKI J, SATYA A T, et al. The pressure induced insulator to metal transition in $FeSb_2$[J]. J. Phys.: Condens. Matter, 2012, 24: 075601.

[47] WANG L V, DENG L, QIN J M, JIA X P. Enhanced thermoelectric properties of double-filled $CoSb_3$ via high-pressure regulating[J]. Inorg. Chem., 2018, 57: 6762.

[48] XIA K, GAO H, LIU C, et al. A novel superhard tungsten nitride predicted by machine-learning accelerated crystal structure search[J]. Science Bulletin, 2018, 63: 817.

[49] GAO H, WANG J J, HAN Y, SUN J. Enhancing crystal structure prediction by decomposition and evolution schemes based on graph theory[J]. Fundamental Research, 2021, 1: 466.

[50] LIU C, GAO H, WANG Y, et al. Multiple superionic states in helium–water compounds[J]. Nat. Phys., 2019, 15: 1065.

[51] XIA K, YUAN J, ZHENG X, et al. Predictions on high-power trivalent metal pentazolate salts[J]. J. Phys. Chem. Lett., 2019, 10: 6166.

[52] GAO H, LIU C, HERMANN A, et al. Coexistence of plastic and partially diffusive phases in a helium-methane compound[J]. Natl. Sci. Rev., 2020, 7: 1540.

[53] LIU C, SHI J, GAO H, et al. Mixed coordination silica at megabar pressure[J]. Phys. Rev. Lett., 2021, 126: 035701.

[54] GAO H, LIU C, SHI J, et al. Superionic silica-water and silica-hydrogen compounds in the deep interiors of Uranus and Neptune[J]. Phys. Rev. Lett., 2022, 128: 035702.

[55] BLÖCHL P E. Projector augmented-wave method[J]. Phys. Rev. B, 1994, 50: 17953.

[56] KRESSE G, FURTHMÜLLER J. Efficiency of *ab-initio* total energy calculations for metals and semiconductors using a plane-wave basis set[J]. Comp. Mater. Sci., 1996, 6: 15.

[57] PERDEW J P, BURKE K, ERNZERHOF M. Generalized gradient approximation made simple[J]. Phys. Rev. Lett., 1996, 77: 3865.

[58] MOMMA K, IZUMI F. VESTA 3 for three-dimensional visualization of crystal, volumetric and morphology data[J]. J. Appl. Crystallogr., 2011, 44: 1272.

[59] TOGO A, OBA F, TANAKA I. First-principles calculations of the ferroelastic transition between rutile-type and $CaCl_2$-type SiO_2 at high pressures[J]. Phys. Rev. B, 2008, 78: 134106.

[60] GIANNOZZI P, BARONI S, BONINI N, et al. QUANTUM espresso: a modular and open-source software project for quantum simulations of materials[J]. J. Phys.: Condens. Matter, 2009, 21: 395502.

[61] MOSTOFI A A, YATES J R, LEE Y S, et al. Wannier90: a tool for obtaining maximally-localised wannier functions[J]. Comp. Phys. Commun., 2008, 178: 685.

[62] SANCHO M P L, SANCHO J M L, RUBIO J. Highly convergent schemes for the calculation of bulk and surface green functions[J]. J. Phys. F: Met. Phys., 1985, 15: 851.

[63] WU Q, ZHANG S, SONG H F, et al. WannierTools: an open-source software package for novel topological materials[J]. Comp. Phys. Commun., 2018, 224: 405.

RuX_2 (X=P、As、Sb) 家族化合物中的压力诱导的超导和拓扑相变

陈　群[1]，吴珏霏[2]，王晓梦[1]，丁　弛[1]，黄天衡[1]，鲁　清[1]，孙　建[1,3*]

1. 南京大学物理学院，固体微结构物理国家重点实验室，南京 210093
2. 上海科技大学物质科学与技术学院，上海 201210
3. 人工微结构科学与技术协同创新中心，南京大学，南京 210093

摘要：作为热电材料 $FeSb_2$ 的姊妹材料，$RuSb_2$ 被广泛研究，但以前的工作主要集中在与 $FeSb_2$ 的比较上，尚未对 $RuSb_2$ 在压力下的性质进行深入研究。在本文中，我们研究了 $RuSb_2$ 在压力下的性质，并探讨了其与 Ru 的磷族化合物 RuP_2 和 $RuAs_2$ 之间晶体和电子结构的异同。我们用晶体结构搜索方法结合第一性原理计算，发现该族化合物经历了一系列结构相变：(I) $RuSb_2$：$Pnnm \rightarrow I4/mcm \rightarrow I4/mmm$；(II) RuP_2：$Pnnm \rightarrow I4_1/amd \rightarrow Cmcm$；(III) $RuAs_2$：$Pnnm \rightarrow P\text{-}62m$。新发现的五个相在高压下都是热力学和动力学稳定的，并表现出金属性。$RuSb_2$ 和 RuP_2 的四个高压相在泄压到零压后动力学依旧稳定。我们计算得到 $RuSb_2$ 的 $I4/mcm$ 和 $I4/mmm$ 相以及 RuP_2 的 $I4_1/amd$ 和 $Cmcm$ 相的超导转变温度在 0 GPa 时分别约为 7.3 K、10.9 K、13.0 K 和 10.1 K。另外，$RuSb_2$ 的 $I4/mcm$ 和 $I4/mmm$ 相以及 RuP_2 的 $I4_1/amd$ 相还具有拓扑非平庸的表面态。我们的研究表明，压力是调节 Ru 的磷族化合物结构、电子和超导性质的有效方法。

关键词：高压；结构搜索；相变；超导电性；拓扑材料

* E-mail: jiansun@nju.edu.cn